Research Square

Preprints are preliminary reports that have not undergone peer review.
They should not be considered conclusive, used to inform clinical practice,
or referenced by the media as validated information.

Machine Learning-Driven Scaffold Hopping Identifies a Non-Classical GSK-3β Inhibitor with Potent Anti-Inflammatory Efficacy

Shiqi Cheng
Army Medical University
Wenyuan Zhang
Army Medical University
Jinjing Zhou
Chongqing University of Science and Technology
Yang Su
Chongqing University of Science and Technology
Jiaming Li
Army Medical University
Dan Peng
Army Medical University
Fang Liu
Army Medical University
Liqun Yang
Southwest University
Shuchen Pei
Chongqing University of Science and Technology
Yao Liu
liuyao@tmmu.edu.cn

Army Medical University

Research Article

Keywords: Glycogen synthase kinase-3β, Machine learning, Random Forest, Virtual screen, Kinase inhibitor, Anti-inflammatory

Posted Date: May 28th, 2026

DOI: https://doi.org/10.21203/rs.3.rs-9640139/v1

License: This work is licensed under a Creative Commons Attribution 4.0 International License.
Read Full License

Additional Declarations: No competing interests reported.

Abstract

This research presents an efficient machine learning-based computational pipeline aimed at the discovery of novel Glycogen Synthase Kinase-3β (GSK-3β) inhibitors. A Random Forest (RF) classification model was created using a carefully chosen set of confirmed inhibitors from 2016 to 2024. The optimized RF model was very strong and accurate (Accuracy: 0.89; AUC-ROC: 0.91 ± 0.02), making it a great first filter for finding chemicals in large spaces. We using this classifier on a new library (Asinex) to obtain the promising candidates, which then went through a series of steps, including ADMET filtering, molecular docking, and molecular dynamics (MD) simulations. The pipeline found two good candidates, RF03 and RF05. In vitro enzymatic assays demonstrated moderate GSK-3β target engagement, producing IC_{50} values of 85.04 μM and 58.73 μM, respectively. The most important thing is that the lead hit, RF05, which has a non-classical, sterically hindered aromatic ester scaffold, worked very well at the cellular level. More biological tests showed that RF05 greatly lowers the levels of pro-inflammatory cytokines (TNF-α and IL-6) while keeping low cytotoxicity. We suggest that this unique chemotype's high lipophilicity and structural pre-organization make it easier for cells to pass through membranes and build up inside cells, turning a moderate biochemical affinity into a strong phenotypic response. This validated computational strategy significantly reduces experimental attrition. Compound RF05 is a potential lead scaffold that gives a structurally different base for the rational design of new anti-inflammatory drugs.

Introduction

Glycogen synthase kinase 3 (GSK-3) is a highly conserved serine/threonine protein kinase ubiquitous in eukaryotic organisms [1]. In mammals, GSK-3 has two distinct isoforms, GSK-3α (51 kDa) and GSK-3β (47 kDa), which share 98% sequence homology within their catalytic domains but diverge significantly at their N- and C-termini [2]. Structurally, GSK-3 comprises two principal functional domains: a substrate-binding domain that facilitates substrate recruitment, and a kinase domain responsible for catalyzing phosphorylation. The catalytic activity of GSK-3 is tightly regulated via phosphorylation at specific residues: activation is mediated by phosphorylation of Tyr279 (GSK-3α) and Tyr216 (GSK-3β), whereas inhibition is mediated through phosphorylation at Ser21 (GSK-3α) or Ser9 (GSK-3β) [3]. Recent studies have primarily concentrated on the GSK-3β isoform because of its complex structural regulation and its pivotal function in essential cellular processes [4]. Extensive research has established that GSK-3β orchestrates multiple critical pathways, such as insulin, neurotrophic factor signaling, Wnt/β-catenin, PI3K/Akt, NF-κB, Reelin, Hedgehog, and Notch signaling [5]. GSK-3β serves as a key regulator of many important cellular processes, including energy metabolism, intracellular signaling, vesicular transport, apoptosis, and proliferation [6]. Aberrant GSK-3β activity is mechanistically implicated in the pathogenesis of diverse human disorders, ranging from neurodegenerative conditions like Alzheimer's disease (AD) [7] to metabolic syndromes such as diabetes mellitus [8], as well as colorectal cancer [9] and rheumatoid arthritis [10]. Notably, emerging evidence increasingly highlights its crucial role in modulating immune responses through the regulation of pro-inflammatory cytokines [11–13]. Hence, it's important to obtain effective GSK-3β inhibitors.

Even though the field of GSK-3β inhibitor development has changed quickly, it is still very hard to turn these drugs into real-life treatments. For instance, Tideglusib, a non-ATP competitive inhibitor, has advanced to Phase II clinical trials for AD [14]. It also exhibited potential therapeutic effects for Parkinson's disease (PD) [15], amyotrophic lateral sclerosis [16], and ischemic stroke [17]. Besides, numerous novel GSK-3 inhibitors have been designed and synthesized in recent years [18–22]. However, the majority of these candidates, predominantly found through traditional high-throughput screening or derivative synthesis. And most of them have stopped moving forward in clinical trials due to off-target toxicity, poor pharmacokinetic profiles, or insufficient isoform selectivity. Therefore, exploring entirely new chemical spaces to identify novel inhibitor scaffolds remains a critical imperative.

To overcome the bottleneck of traditional screening, machine learning (ML)-based virtual screening has emerged as a new way for rational drug design. ML methods greatly improve the speed of screening and the ability to search through large unexplored chemical libraries. Ensemble learning algorithms like Random Forest (RF) are especially useful for targets with complicated structures, like GSK-3β, where traditional pharmacophore models often miss small structural changes [23]. RF models are highly resistant to overfitting, adept at managing high-dimensional molecular descriptors, and offer interpretable insights into feature importance [24]. In light of this reason, we created a computational pipeline driven by RF to virtually screen for new GSK-3β inhibitors. This study seeks to identify novel chemical scaffolds characterized by balanced physicochemical properties and advantageous cellular phenotypes, rather than exclusively focusing on extreme enzymatic affinity. The predictive robustness of the model and the multi-target anti-inflammatory potential of the identified hits were subsequently substantiated through rigorous in vitro and cellular experimental validation.

Materials and Methods

Data Curation and Preprocessing.

The compound library utilized for model construction was meticulously curated from public and commercial databases, including PubChem [25] and TargetMol, and further enhanced by data sourced from peer-reviewed literature published between 2016 and 2024 (Fig. 1A). We collected 714 compounds that had different bioactivity units, such as IC_{50}, Ki, EC_{50}, and KD. A set of experimentally confirmed GSK-3β inhibitors was compiled, with standard SMILES notations and corresponding IC_{50} values systematically obtained from public databases. We used ChemDraw 20.0 to make standardized SMILES strings for compounds that didn't have clear structural identifiers. We used strict curation to get rid of duplicates, entries with missing or unclear activity measurements, and structures with inconsistent stereochemistry or valency. We put each compound into one of two groups: the positive class (labeled "1") was made up of inhibitors that had been tested and found to work, and the negative class (labeled "0") was made up of compounds that we knew were not active.

Molecular Featurization and Descriptors Calculation.

In the initial phase of model development, we leveraged a custom implementation of calculate_descriptors() to get a standard set of 208 two-dimensional molecular descriptors from RDKit [26]. These descriptors included molecular weight, ring count, hydrogen bond donors and acceptors, and Kier & Hall [27] topological indices. We got these descriptors directly from SMILES-derived molecular graphs. This transformation converted discrete molecular representations into fixed-length numerical feature vectors. Then, Min–Max normalization was applied to mitigate scaling disparities across features. The next steps were data consolidation, stratified train-test splitting, hyperparameter tuning, and model evaluation. These were all executed in a Jupyter Notebook [28] environment to ensure reproducibility and facilitate iterative analysis. The engineered feature set has two main types of descriptors: Structural Descriptors and Topological Descriptors. These measure molecular connectivity and scaffold architecture, including bond and atom counts, ring systems, and topological indices. Physicochemical, Electronic, and Geometric Descriptors, capturing properties critical to molecular behavior and interactions, such as lipophilicity (Log P), topological polar surface area (TPSA), molar refractivity, and electronic profile characteristics. It is important to note that all geometric and electronic descriptors were only based on 2D molecular representations. No 3D conformation generation or quantum-chemical optimization was used, because it was more efficient and fit better with standard cheminformatics pipelines.

Random Forest Classifier: Development and Hyperparameter Optimization.

The complete dataset was partitioned into training (80%) and independent test (20%) sets using stratified random sampling to maintain the original class distribution. The training set was used for model development and hyperparameter tuning, whereas the test set was reserved for unbiased evaluation of the model's generalization capability. We employed a Random Forest algorithm and set the hyperparameter search space to include n_estimators (range: 100–180) and max_depth (range: 10–40). All other parameters were set to their default values in scikit-learn.Confusion matrix analysis indicated a high false positive rate and a low recall, which helped improve the model. By systematically comparing evaluation metrics across different combinations of hyperparameters, we were able to find the best configuration that gave us a good balance of precision, recall, and accuracy.

Predictive Model Validation and Evaluation.

In order to comprehensively evaluate the model performance, we adopt Precision, Recall and Accuracy as quantitative metrics and introduce Confusion Matrix as a visualization tool. Precision, Recall and Accuracy are defined as follows:

$$\text{Precision} = TP/(TP + FP)$$

$$\text{Recall} = TP/(TP + FN)$$

$$\text{Accuracy}=(TP + TN)/(TP + TN+FP + FN)$$

F1Score = 2 × (Precision × Recall)/(Precision + Recall)

Within the confusion matrix, True Positives (TP) and True Negatives (TN) correspond to correctly identified active and inactive compounds, respectively. False Positives (FP) denote inactive compounds incorrectly predicted as active, whereas False Negatives (FN) refer to active compounds misclassified as inactive. The metrics Precision and Recall offer complementary perspectives on classifier performance: Precision reflects the reliability of positive predictions, and Recall captures the model's ability to identify all relevant active instances. Accuracy provides an overall measure of classification efficacy, with a value of 1.0 indicating perfect discrimination, 0.5 equivalent to random guessing, and results below 0.5 suggestive of systematic misclassification. The model was rigorously assessed on an independent test set through detailed metric evaluation, supported by ROC curve analysis and inspection of the confusion matrix.

Virtual Screening.

Following model optimization and evaluation, the optimized Random Forest classifier was used to conduct virtual screening of a commercially available compound library (Asinex Database; n = 575,302 compounds) (Fig. 1B). A standardized computational pipeline was used to process the canonical SMILES strings for each compound. This created molecular fingerprints and descriptors, which were then fed into the trained model. Based on the classifier's output, compounds that were predicted to be active against GSK-3β were given priority for further experimental validation.

Toxicity Prediction.

Toxicological profiling of the computationally prioritized GSK-3β inhibitor candidates was conducted using Toxtree (v3.1.0) [29]. There are three main steps in the assessment workflow: First, automated structural normalization was used to fix stereochemical problems and make sure that canonical SMILES representations followed the rules of Cramer. Second, the software's recursive fragment-based algorithm was used to put compounds into Cramer's structural classes in a systematic way. Finally, complete toxicity profiles were made that included Cramer classifications, estimated Threshold of Toxicological Concern (TTC) values, annotated rule-based pathways, and pictures of important structural features.

Theoretical Prediction of the ADME Properties.

In silico ADME (Absorption, Distribution, Metabolism, and Excretion) profiling was conducted at the lead prioritization stage using ADMETlab 3.0 [30]. The platform received systematic submissions of canonical SMILES representations of candidate compounds. A complete set of 119 pharmacokinetic and toxicological endpoints was evaluated simultaneously to enable a unified assessment of compound developability.

Molecular Docking.

Molecular docking studies were conducted using AutoDock Vina (v1.2.7) [31, 32] to evaluate binding affinities between prioritized compounds and the GSK-3β kinase ATP-binding site. Structure preparation was conducted using AutoDock Tools (v1.5.7). The protein receptor (PDB ID: 7B6F)[33] was kept as a stiff structure, and the ligand was treated as flexible by defining rotatable torsion bonds. The Kollman and Gasteiger methods were used to give the receptor and ligand partial atomic charges. After that, docking was done using the Lamarckian Genetic Algorithm (LGA) and pre-calculated grid maps. The AutoGrid program made the grid box, which is 35 × 35 × 35 Å in size and is centered at (x, y, z) = -0.839, 5.006, 22.148. The number of docking runs was set to 50, and all the other settings were left the same. We used PyMOL to look at the data in 3D and LigPlot+ to look at it in 2D to see how ligands and proteins interact after docking.

Molecular Dynamics Simulations.

Molecular dynamics (MD) technique is on the verge of becoming standard computational tools for drug discovery. MD simulations were conducted using GROMACS program version 2023.2. In this study, the Sobtop Server (http://sobereva.com/soft/Sobtop; Version 1) was utilized to generate CHARMM input topology files. The CHARMM 36 force field was employed for both proteins and the ligands. The TIP3P water model was used to solvate the protein-ligand complexes in a dodecahedral box. The distance between the solute and the edges of the box was at least 10 Å. The system charge was neutralized by the addition of appropriate counter-ions. Following the system assembly, all of the settings went through energy minimization using the steepest descent method for 10,000 steps. Then, a 10 ns equilibration phase was created at 310 K, with the number of atoms, volume, and temperature (NVT) staying the same. Then, there was an unconstrained MD simulation that lasted 100 ns in the NPT ensemble, where the number of particles, pressure, and temperature stayed the same. The temperature stayed at 310 K and the pressure stayed at 1 atm. To keep the covalent bonds in the protein the same length, we used LINCS (Linear Constraint Solver) restrictions. The simulations were merged at a time step of 2 fs, and the initial unfavorable energy state was changed into a new one with a cutoff of 1.2 nm for both Coulomb and Lennard-Jones interactions. Trajectory analyses encompassed the computation of hydrogen bonds, Root Mean Square Deviation (RMSD), Solvent Accessible Surface Area (SASA), Radius of Gyration (Rg), and Root Mean Square Fluctuation (RMSF). We also used the gmx covar and gmx anaeig modules to do Principal Component Analysis (PCA) and Free Energy Landscape (FEL) analyses. The covariance matrix was diagonalized to get the principal component projections[34].

Kinase Inhibition Activity Assay.

Inhibition of GSK-3β kinase activity by the compounds was assessed using the Kinase-Glo® Luminescent Kinase Assay kit (Promega, V6711). Assays were performed in opaque-walled 96-well plates (Corning 3912) with a total reaction volume of 40 µL per well. Each well received 10 µL of the target compound at a concentration gradient (3.13 µM, 12.5 µM, 25 µM, 50 µM, 100 µM, and 200 µM), followed by sequential addition of 2 ng of recombinant human GSK-3β kinase and 20 µL of reaction buffer containing 4 µM ATP and 12.5 µM substrate peptide (sequence:

YRRAAVPPSPSLSRHSSPHQ(pS)EDEEE). The negative control was LiCl, and the positive control was just thesame volume of assay buffer. After 30 minutes of incubation at 30°C, the addition of 40 μL of Kinase-Glo® reagent stopped the enzymatic reactions. Luminescence (Relative Light Units, RLU) was measured using a SYNERGY H1 microplate reader (BioTek Instruments, Inc.). The percentage inhibition was calculated according to the formula: Inhibition (%) = 100 × (RLU (neg)-RLU (cpd)) / (RLU (neg)-RLU (pos)), where RLU (neg) represents the luminescence of the negative control (LiCl, defining maximum enzyme activity) and RLU (pos) represents the luminescence of the positive control (buffer only, defining background). Raw data were normalized to control well values. Concentration-response curves were generated by plotting inhibition percentages against compound concentration and subjected to nonlinear regression analysis using GraphPad Prism software (version 10.1.2) to determine the half-maximal inhibitory concentration (IC_{50}).

Cell Counting Kit-8 (CCK-8).

In vitro cytotoxicity of compounds RF03 and RF05 was evaluated using RAW264.7 murine macrophages. Cells were placed in complete medium (ZQXZ Biotech, ZM0098) at a density of 1×10^4 cells per well and kept at 37°C with 5% CO_2 for 24 hours. Subsequently, the cells were treated with RF03 and RF05 at concentrations of 2.5–80 μM for another 24h respectively. Cell viability was determined using the CCK-8 assay kit (MCE, HY-K0301). After incubating with the reagent for 1 h, the absorbance at 450 nm was measured using a SYNERGY H1 microplate reader. The results are shown as the mean ± standard deviation from three separate experiments, with the vehicle-treated control groups used as a baseline.

Enzyme-Linked Immunosorbent Assay (ELISA).

The anti-inflammatory activity was evaluated using lipopolysaccharide (LPS)-stimulated RAW264.7 macrophage cells. Cells were plated in 24-well culture plates at a density of 5×10^5 cells per well and allowed to adhere overnight at 37°C. After removal of the supernatant, the cells were treated in triplicate with one of the following: culture medium (negative control), 1 μg/mL LPS alone, 1 μg/mL LPS plus 10 μM Tideglusib (positive control), or 1 μg/mL LPS together with 40 μM of the test compound RF03 and RF05. Following treatment, the plates were incubated for 24 hours at 37°C under 5% CO_2 to induce inflammatory activation. Subsequently, the supernatant was collected by centrifugation at 3,000 rpm for 20 minutes, and the levels of the pro-inflammatory cytokines TNF-α and IL-6, as well as the anti-inflammatory cytokine IL-10 were quantified using a commercial ELISA kit (Animaluni).

Statistics.

Statistical analysis was performed using GraphPad Prism 10.1.2 software. Data results are expressed as mean ± standard error (mean ± SEM). Significant differences between groups were evaluated using analysis of variance (ANOVA), with $P < 0.001$ regarded as statistically significant.

Results and Discussion

Comprehensive Model Performance Assessment.

Conventional machine learning approaches use abundant data to predict new drug outcomes by learning latent patterns within relevant information. Some of the most popular methods include Random Forest (RF), Support Vector Machines (SVMs) [35], k-Nearest Neighbors (KNN) [36], Naive Bayes (NB) [37], and Gradient boosting (GB) [38]. In this study, a prediction model was developed utilizing the Random Forest algorithm and subsequently optimized to improve its predictive efficacy.

To thoroughly evaluate the predictive stability and generalization capacity of the developed RF model, we performed a lateral performance evaluation using two independent validation cohorts: an initial “Limited Validation Set” (n = 91) and a more extensive “Extended Validation Set” (n = 266). In the initial assessment (n = 91; 47 active, 44 inactive), the model exhibited a conservative classification approach. The accuracy was good at 0.892, which means that the false discovery rate was low. However, the recall was only at 0.702 (Fig. 2A). The confusion matrix showed 14 false negatives (Fig. 2B), which means that the model had trouble finding some "hard-to-classify" active edge cases in this small chemical space. This caused a miss rate of about 30%. When the validation scope was broadened to include the structurally diverse Extended Validation Set (n = 266; 136 active, 130 inactive), there were significant improvements in all of the key performance metrics (Fig. 2C, 2D). The RF model demonstrated robust generalization, with the precision went up from 0.892 to 0.921 (Fig. 2C). Mover, the recall rate went up from 0.702 to 0.853, which cut the false negative rate in half, from about 30% to about 14.7% (Fig. 2C). This recovery shows that the model's decision boundaries are clear and can pick up most active scaffolds when given a representative sample distribution. The F1-score went up from 0.786 to 0.885, which shows that the balance between precision and sensitivity was just right. During both validation phases, the model maintained a specificity consistently above 90% (False Positive Rate < 8%). The stability of this metric, combined with the significant enhancements in sensitivity during scaling, validates that the RF model is not only statistically sound but also exceptionally dependable for the effective virtual screening of GSK-3β inhibitors from extensive compound libraries. Salvatore *et al.* used a hybrid model that combined RF and KNN, which improved accuracy to 0.71 and precision to 0.65. This integrated model was able to identify GSK-3β inhibitors G1 and G [39]. Pirzada *et al.* construct a model was capable of identifying and repurposing already approved drugs targeting the specified GSK-3 using histogram-based gradient boosting (HGBM) and light gradient boost machine (LGBM) algorithms [40]. A comparative analysis indicating that our RF model demonstrates superior performance.

A 5-fold cross-validation method was used to evaluate the model performance [41]. In the combined Receiver Operating Characteristic (ROC) curve (Fig. 3A), the RF model achieved a compelling ROC-AUC of 0.91 ± 0.02, with peak performance reaching 0.938 in individual folds (Fig. 3B). In the context of binary classification for drug discovery, an AUC exceeding 0.9 indicates a model with excellent discriminative power between active and inactive compounds. Patricia et al. developed a machine learning model using a Bayesian algorithm to find GSK-3β inhibitors. This model got an ROC of 0.905 under five-fold cross-validation [42]. A comparative evaluation demonstrates that our RF model has distinct performance

superiority. Precision is essential for practical drug discovery, which can reduce the substantial costs of downstream chemical synthesis and biological assays. The RF model achieved a Precision of 0.927 (Fig. 3B), implying that approximately 93% of the compounds predicted as active are true inhibitors. Besides, it has a Recall of 0.838 and an F1-Score of 0.880, showing that the classifier is very efficient (Fig. 3B). The model achieved a remarkable AUC-PR (Area Under the Precision-Recall Curve) of 0.950 (Fig. 3B). As PR-AUC is the definitive metric for imbalanced datasets, this score confirms the model can effectively capture the characteristics of positive samples without being biased by the negative majority. A Matthews Correlation Coefficient (MCC) of 0.771 further confirms that the model maintains a strong positive correlation between predicted and observed classifications. The RF model represent the top tier of performance, significantly outperforming Logistic Regression, K-Nearest Neighbors, Decision Trees, and Naive Bayes classifiers (Fig. 3C,3D).

Physicochemical Interpretability and Mechanistic Alignment.

In addition to being able to make accurate predictions, a model that can be used in practice must show medicinal chemistry logics. Figure 3E shows the identified top 20 most important molecular features through Random Forest model. Table 1 gives a quantitative summary of these features. These descriptors encompass various essential physicochemical domains, including electronic properties and charge distribution, topological structure indices, surface property descriptors, and metrics related to molecular volume, polarizability, and hydrophobicity.

The BCUT2D_CHGHI (molecular surface charge/polarity extremes) descriptor had the highest feature weight, which means that the best small molecule compounds have strong cationic properties. The GSK-3β ATP-binding pocket has an electrostatically complementary environment with anionic residues, such as Asp133 and Tyr134, which makes it easier for molecules to bind. This makes it more likely that charge-based interactions will happen. The VSA_EState2 and VSA_EState8 descriptors show that polar and hydrogen-bonding pharmacophores on the surface of molecules are also connected to stronger inhibitory activity. These functional groups are very important for making hydrogen bonds with polar residues in the binding site, like Thr138 and Gln185. The FpDensityMorgan3 descriptor showed the importance of wide electron density. This suggests strong inhibitors usually have pharmacophores with complicated structures. Moreover, atomic polarizability (Avglpc) suggests that electronic distribution can improve affinity. This electronic property probably makes the binding pocket to interact with aromatic residues like Phe67 and Tyr216 in a good way through π–π stacking or cation–π interactions.

These results demonstrate that effective inhibitors require pharmacophores with intricate structures, typically comprising polycyclic core systems or diverse substitution patterns. GSK-3 is a kinase that usually needs specific polar interactions, like hydrogen bonding at the hinge region, and hydrophobic interaction. These insights align with the existed inhibitor scaffolds, including indolocarbazoles and aminopyrimidines, wherein localized pharmacophore diversity is crucial for effective target binding.

However, the correlation matrix (Fig. 3F) shows that the feature importance scores are too similar to each other, which makes it harder to see the basic mechanistic drivers. Figure 3A–3F elucidate the RF

model efficiency be used to screen for GSK-3β inhibitors. The current RF model is ready to be used in virtual screening campaigns, like ZINC or internal libraries. It is a good way to filter out inactive compounds because it has a high accuracy and a high AUC-PR. This makes the best use of resources for wet-lab validation. The RF model shows that it can make accurate predictions for all of the most important performance indicators. As a result, the model can find possible GSK-3β inhibitors in large compound libraries with a high level of accuracy.

Table 1
Key descriptors in constructed RF model.

Feature category	Number of descriptors	Representative descriptors
Charge and Electronic Properties	5	BCUT2D_CHGHI, BCUT2D_CHGLO, MaxPartialCharge, MinAbsPartialCharge, MiniEStateIndex
Topological Characterization	6	SPS, Kappa3, RingCount, FpDensityMorgan2, FpDensityMorgan3, HallKierAlpha
Surface Property Characterization	5	VSA_EState2, VSA_EState8, SlogP_VSA8, PEOE_VSA7, SMR_VSA6
Volume, Polarizability, and Hydrophobic Properties	4	Avglpc, BCUT2D_MRLOW, BCUT2D_LOGPLOW, BCUT2D_MRHI

Virtual Screening.

Using the validated Random Forest model, virtual screening identified 97,459 possible GSK-3β inhibitors in the Asinex commercial compound library (n = 575,302), which is a hit rate of 16.9%.

Theoretical prediction of the ADME properties.

We next use Toxtree for toxicological evaluation, 54 out of 97,459 candidate molecules were predicted as Cramer Classes I or II, which means they have a low or moderate risk of being toxic. The other compounds were put into Cramer Class III, which means they have a high risk of being toxic. Consistent with the safety-first principle in drug discovery, all Class III compounds were excluded from further consideration. The retained subset of 54 compounds, which exhibit favorable toxicity profiles, will proceed to subsequent developability assessments alongside evaluation of their GSK-3β inhibitory activity. To narrow down an initial pool of 54 compounds, we used a two-phase funneling strategy based on ADMET predictions from ADMETlab 3.0. Initially (Phase 1), candidates were subjected to a quantitative scoring system that balanced key properties including intestinal absorption (Caco-2, LogP), distribution (PPB, VDss), and metabolic stability (CYP450 inhibition). Subsequently (Phase 2), the top-scoring compounds were further curated based on structural diversity and synthetic accessibility to yield a final selection of 18 promising candidates for further experimental validation. The compounds possess acceptable physicochemical and ADME parameters were summarized in Table 2. All compounds except RF02, RF08, RF10, RF12, and RF17 had Caco-2 permeability values greater than −

5.15. This means that these compounds have good intestinal permeability and absorption properties. The LogP values for all compounds fall within the range of 1–5, consistent with Lipinski's Rule. At the same time, all of the compounds possessed adequate systemic distribution characteristics. Plasma clearance (CLplasma) is a critical pharmacokinetic parameter. Predictive analysis indicated that all compounds exhibited favorable plasma clearance properties.

Table 2
ADMET prediction results of compounds using ADMETlab 3.0

Cpds	Absorption		Distribution		Metabolism		Excretion	
	Caco-2 Permeability (logPapp in 10^{-6} cm/s)	LogP	PPB (%)	VDss (L/kg)	CYP substrate	CYP inhibitor	CL_{plasma} (ml/min/kg)	$T_{1/2}$ (h)
RF01	-4.857	1.498	92.6	0.849	1A2 2D6 2B6	1A2 2D6 2B6 2C8	10.59	1.081
RF02	-5.363	2.224	88.4	0.929	1A2 2D6 2B6	1A2 2C9 2D6 2B6 2C8	8.351	1.018
RF03	-4.845	4.519	98.2	1.303	1A2 2C9 2D6 3A4	2D6	3.408	0.983
RF04	-4.371	2.701	98.2	0.36	2C19 2C9 2D62B6	1A2 2D6	1.888	0.626
RF05	-4.818	4.826	98.4	1.995	2C9 2D6 2B6	1A2 2D6	7.358	0.348
RF06	-4.882	2.984	77.5	0.689	1A2 2C19 2C9 2D6 3A4 2B6	2D6 3A4 2B6	8.547	0.63
RF07	-4.866	1.733	86.9	1.06	1A2 2C19 2C9 2D6 2B6	1A2 2B6 2C192C9 2D6 3A4	5.937	0.562
RF08	-5.417	3.875	92.8	1.245	1A2 2C19 2C9 2D6 3A4 2B6	2D6 3A4 2B6	5.764	0.606
RF09	-5.139	3.556	87.0	3.274	1A2 2C19 2B6 2C9 3A4 2D6	1A2 2D6 3A4	7.135	0.305
RF10	-5.322	0.451	97.4	0.219	1A2 2C19 2D6 3A4 2B6	1A2 2C19 2C9 2D6 3A4 2B6 2C8	1.787	0.99
RF11	-5.139	3.556	87.0	3.274	1A2 2C19 2C9 2D6 3A4 2B6	2D6 1A2 3A4	7.135	0.305
RF12	-5.763	0.006	98.5	0.184	1A2 2C19 2C9 2D6 3A4 2B6	1A2 2C19 2C9 2D6 3A4 2B6	0.88	1.658

Cpds	Absorption		Distribution		Metabolism		Excretion	
	Caco-2 Permeability (logPapp in 10^{-6} cm/s)	LogP	PPB (%)	VDss (L/kg)	CYP substrate	CYP inhibitor	CL_{plasma} (ml/min/kg)	$T_{1/2}$ (h)
RF13	-4.758	3.207	97.5	0.258	1A2 2C19 2C9 3A4 2B6	1A2 2C9 2D6 3A4 2B6 2C8	5.569	0.527
RF14	-4.985	4.522	66.4	4.115	1A2 3A4	1A2 2C9	9.129	0.234
RF15	-4.718	2.801	95.7	0.37	1A2 2C19 2C9 2D6 2B6	2D6 2B6	4.757	0.865
RF16	-4.925	2.052	96.7	2.504	1A2 2C19 2C9 2D6 3A4 2B6	2D6 3A4 2B6	6.482	0.711
RF17	-5.478	0.6	95.7	0.894	1A2 2C19 2C9 2D6 3A4 2B6	1A2 2C19 2C9 2D6 3A4 2B6 2C8	4.11	1.282
RF18	-4.492	2.085	96.4	0.838	2C19 2C9 2D6 3A4 2B6	2C19 2C9 2D6 3A4 2B6 2C8	5.011	0.998

Multiparametric radar visualization of compound drug-like attributes was systematically profiled using ADMETlab 3.0 computational platform. The bioavailability radar graphic shows that the bioavailability of substances may be attributed to their ideal physicochemical properties. These charts show 13 critical parameters, reflecting appropriate molecular weight, balanced lipophilicity (as indicated by logP/logD), adequate aqueous solubility (logS), optimal hydrogen bonding potential (the number of hydrogen bond acceptors, nHA; the number of hydrogen bond donors, nHD), and suitable modulation of molecular flexibility/rigidity (the number of rotatable bonds, nRot; nRig). The orange, blue, and green polygons show the actual properties of the compound, the lower limits of the parameters, and the upper limits of the parameters. As shown in Fig. 4, all of the top 18 compounds' physicochemical parameters (orange polygon) were within the best ranges, which means they were compatible with the basic principles of drug-likeness in medicinal chemistry.

Molecular Docking.

In this study, we utilized molecular docking to obtain a better understanding of the potential interactions between inhibitors and GSK-3β. The binding energy during the interaction of candidates with the GSK-3β structure is shown in Table 3. Palomo *et al.* previously utilized fpocket to survey the surface of GSK-3β, identifying seven pockets. These are divided into groups: the canonical ATP-binding site, the substrate-binding site, the Axin/FRAT tide binding site, three allosteric sites (designated pockets 4, 5, and 7), and

an orphan pocket (pocket 6) [43]. As presented in Fig. 5A-5P, eight compounds make hydrophobic interactions with GSK-3β through major residues such as Ile62, Gly63, Gly65, Val70, Ala83, Asp133, Tyr134, Asn186, Leu188, Cys 199, and Asp200, revealing conserved interactions with the same set of residues. Their docking against the ATP-binding pocket of GSK-3β, indicating that all of the ligands may be regarded as strong competitive inhibitors as they can all compete with ATP. In addition, extensive studies demonstrate that hydrophobic interactions not only enhance ligand-protein binding affinity but also facilitate a subsequent increase in biological potency [44–46].

The molecular docking results showed that RF03 (Fig. 5E, 5F) had an affinity of -9.035 kcal/mol, which is interesting. Figure 5E and 5F showed that its interaction network is mostly hydrophobic and has twelve residues: Lys 85, Asp 200, Phe67, Val70, Thr138, Lle62, Val135, Leu188, Ala83, Val110, Leu132, and Cys199. RF05 had the lowest negative binding energy (-9.035 kcal/mol) of all the chemicals, which means it had a better binding affinity. The binding mode analysis reveals that RF05 forms one hydrogen bond with residue Cys199 and ten hydrophobic interactions with Glu97, Lys85, Val70, Ile62, Val135, Leu188, Asp133, Val110, Leu132, and Asp200 (Fig. 5I, 5J).

Table 3
Calculated docking binding energies of compounds with GSK-3β structure protein and interactions formed by binding residues with ligand.

Cpds	Binding energy (kcal/mol)	Residues involving binding interactions
RF01	-7.523	Asp200, Glu97, Val110, Leu132, Lys85, Ala83, Leu188, Cys199, Phe67, Asn186, Val70
RF02	-7.677	Tyr140, Gln185, Asn186, Val70, Phe67, Cys199, Ala83, Leu188, Arg141, Thr138
RF03	-9.035	Lys85, Asp200, Phe67, Val70, Thr138, Lle62, Val135, Leu188, Ala83, Val110, Leu132, Cys199
RF04	-8.727	Lys85, Val70, Asp200, Cys199, Tyr134, Pro136, Ile62, Val135, Leu188, Ala83, Val110, Leu132
RF05	-9.169	Cys199; Glu97, Lys85, Val70, Ile62, Val135, Leu188, Asp133, Val110, Leu132, Asp200
RF06	-8.425	Leu132, Lys85, Val110, Val70, Phe67, Lys183, Gln185, Asn186, Asp200, Cys199
RF07	-8.748	Lys85; Val110, Leu132, Cys199, Val70, Gly63, Ile62, Pro136, Val135, Thr138, Phe67, Asn186, Asp200
RF08	-8.627	Lys85; Val110, Leu132, Cys199, Val70, Gly63, Ile62, Pro136, Val135, Thr138, Phe67, Asn186, Asp200

Molecular dynamic simulation.

MD simulations provide a powerful method to investigate atomic-level behavior and system dynamics. To study the structural alterations and dynamic behavior of the protein in complex with two selected ligands, all systems were underwent 100 ns simulation. The RMSD was used to quantify the deviation of the Cα atoms between the initial structure and the final simulated conformation, serving as a key metric for assessing system equilibration and conformational stability. As shown in Fig. 6A, both complexes maintained their global fold stability, with RMSD values consistently staying below the 0.3 nm (3 Å) benchmark typically associated with stable molecular dynamics trajectories. Neither system showed any signs of structural unfolding or ligand dissociation. Hence, both compounds act as potential inhibitors capable of forming stable complexes with GSK-3β.

The RMSF quantifies the fluctuation magnitude of each residue throughout the simulation, thereby delineating local flexible and rigid regions within the protein. This metric complements RMSD by providing residue-level insights that are not accessible from global measurements, enabling the identification of specific loop segments or active-site residues undergoing motion. Figure 6B illustrated that the global fluctuation profiles for both complexes exhibit remarkably similar topologies, with major peaks and troughs lining up across the residue index (residues ~ 30–390). This agreement confirms that ligand binding does not disrupt the fundamental tertiary architecture and secondary structure of the protein in both systems. There is a notable exception near residue ~ 370, where the RF03 complex has a slightly higher fluctuation peak than RF05. This localized enhancement in flexibility may be due to particular induced-fit modifications or steric influences distinctive to the binding mode of RF03 within that subdomain.

To further assess the structural compactness and overall folding stability of the protein-ligand complexes, the Rg was monitored throughout the simulation (Fig. 6C). Stable Rg values indicate that the structure is a compact and well-folded. Rg Values for both systems are confined within a narrow range of 2.11–2.18 nm, which demonstrates both complexes have remarkable stability. These results fit perfectly with the previous structural analyses.

The total SASA was calculated over the 100 ns simulation trajectory (Fig. 6D) to evaluate the changes in the surface exposure of the protein-ligand complexes and assess the stability of the hydrophobic core. The SASA analysis confirms the results from the RMSD and Rg studies. SASA values stayed low during the 40–100 ns simulation phase, fluctuating between 175 nm^2 and 185 nm^2. The mostly overlapping trajectories show that both systems are moving toward a compact conformational state. The SASA result further supports their potential as promising GSK-3β inhibitors.

PCA is primarily utilized for dimensionality reduction analysis of the motion trajectory of protein-ligand complexes during simulation processes. Figure 7A shows that the complex bound to RF03 exhibits a broad and diffuse distribution within the essential subspace. The irregular and scattered morphology of the cluster suggests that the protein undergoes substantial conformational fluctuations and structural rearrangements during the simulation, suggesting that RF03 may not effectively stabilize a specific conformation of the target protein. In contrast, the complex of RF05-GSK-3β (Fig. 7B) displays a very

dense and compact cluster. The conformational sampling is limited to a narrow region, with both PC1 and PC2 values mostly staying between − 0.5 nm and + 0.5 nm, which suggests the complex is structurally rigid and stable. Hence, the comparative analysis demonstrates that the RF05 complex samples a much smaller conformational space than the RF03 complex. Given that potent inhibitors typically function by restricting protein conformational flexibility and stabilizing specific binding poses through rigidification, RF05 is expected to possess superior inhibitory efficacy and higher binding affinity for GSK-3β than RF03.

The FEL plots for RF05 show that it has a stronger binding affinity (Fig. 8). The energy basin for RF05 is relatively narrow and deep, which means that RF05 could keep the complex stable. The stable state of RF05 has a lower RMSD (about 0.18 nm) than RF03 (about 0.23 nm), which means that RF05 capable of keeping binding pocket intact. These results suggests that RF05 is a superior GSK-3β inhibitor than RF03.

CCK8 Assay.

The cytotoxic effect of compound RF03 on RAW264.7 cells was assessed via CCK-8 assay to establish a non-cytotoxic concentration range for further experiments. As illustrated in Fig. 9A and 9B, RF03 and RF05 demonstrated minimal cytotoxicity at 40 μM, which act as a sub-lethal concentration for assessing their anti-inflammatory mechanisms.

Kinase Inhibition Activity Assay.

Kinase-Glo® Luminescent Kinase Assay was used to test inhibitory effect. LiCl used as a control. Figures 9C and 9D show typical dose-response curves for drugs. Robust curve fitting finds that the IC50 of RF03 and RF05 is 85.04 μM and 58.73 μM, respectively (Fig. 9C, 9D). This confirms that RF05 possesses superior direct inhibitory potency compared to RF03, with an approximately 1.45-fold increase in efficacy.

Anti-inflammatory Activity Assay.

To evaluate the anti-inflammatory efficacy of the candidate compounds, we quantified the expression levels of pivotal pro-inflammatory (TNF-α, IL-6) and anti-inflammatory (IL-10) cytokines subsequent to treatment with RF03 and RF05 (40 μM). Tideglusib used as a positive control. The validation of the inflammatory model was substantiated by the significant upregulation of TNF-α and IL-6 in the Model group relative to the Negative Control (NC). Figure 9E demonstrates that all treatment groups significantly diminished TNF-α production compared to the Model group. RF05 had the strongest inhibitory effect, lowering TNF-α levels to about 73.31 pg/mL, which was better than both the RF03 group and the positive control. Besides, RF05, RF03 and Tideglusib also caused a big drop in IL-6 levels (Fig. 9F). The Model group showed a compensatory rise in IL-10 compared to the baseline, but the RF03 treatment caused a clear and large rise in this anti-inflammatory cytokine (Fig. 9G). These results show that RF03 and RF05 both have strong anti-inflammatory effects, but they probably work in different ways.

RF05 primarily inhibit the secretion of pro-inflammatory cytokine synthesis, whereas RF03 appears to increase the secretion of anti-inflammatory cytokine IL-10.

Collectively, the convergence of evidence from molecular docking, MD simulations, conformational sampling (FEL/PCA), and biological activity assay identifies compound RF05 as the most promising hit candidate., RF05 possesses favorable thermodynamic profile and remarkable cellular efficacy. RF descriptor weights and comprehensive structural simulations clarifies the behind mechanism in the RF05 and GSK-3β binding complex. RF05 has a sterically hindered aromatic ester (2,6-dimethylphenyl 2,4,6-trimethylbenzoate), which is different from regular, flat kinase inhibitors that are high in nitrogen. Finding this lipophilic scaffold makes perfect sense of the main predictive features that our RF model found. The model assigned the highest weight to the BCUT2D_CHGHI descriptor (molecular surface charge and polarity extremes). The aromatic rings in RF05 have a lot of electrons, and the ester carbonyl oxygen is only partially buried. This makes a unique, localized electrostatic potential that is very different from the surface, which is mostly hydrophobic. The topological descriptor FpDensityMorgan3 is also very important because it shows the unique three-dimensional geometry of RF05. The five ortho-methyl groups make it hard for the two phenyl rings to move, which keeps them in a rigid, orthogonal (almost perpendicular) shape. This pre-organized topological complexity represents a perfect example of scaffold hopping.

Molecular docking and dynamic simulations perfectly turn these 2D descriptor insights into a 3D binding mechanism. The screened library showed that RF05 exhibited the lowest negative binding energy (-9.169 kcal/mol). The important ester carbonyl oxygen in RF05 is a strong hydrogen bond acceptor. It forms a basic hydrogen bond with Cys199, which is a key interaction in the important hinge region of the GSK-3β ATP-binding pocket. At the same time, the uniquely rigid, orthogonal conformation allows the five peripheral methyl groups to extensively occupy the deep hydrophobic clefts of the active site. This establishes a massive Van der Waals and hydrophobic interaction network engaging ten key residues, including Glu97, Lys85, Val70, Ile62, Val135, Leu188, Asp133, Val110, Leu132, and Asp200. Our FEL and PCA analyses also support the idea of geometric complementarity. RF05 created a very narrow and deep energy basin with a very low RMSD (~ 0.18 nm), which shows that this sterically bulky ester tightly locks the kinase in a stable form without changing its structure. These structural properties of RF05 explain why it has great biological profile. RF05 inhibited GSK-3β moderately *in vitro* (IC_{50} = 58.73 μM), but it had strong anti-inflammatory effects at the cellular level, greatly lowering the levels of TNF-α and IL-6 without harming cells. It perhaps due to the high lipophilicity and its steric effects. These properties let RF05 can easily cross cell membranes and get into macrophages. This pharmacokinetic benefit makes up its in vitro target affinity. Ultimately, these results highlight the exceptional proficiency of our RF model in detecting not only high-affinity in vitro binders but also physiologically relevant, cell-active lead scaffolds primed for further structural enhancement.

Conclusions

In summary, this study establishes a robust and highly efficient machine learning-driven pipeline for the virtual screening and hit discovery of novel GSK-3β inhibitors. Our optimized RF classifier achieved excellent predictive reliability (Accuracy: 89%; AUC-ROC: 0.91 ± 0.02) by using a carefully chosen dataset. It was able to navigate extensive chemical spaces while greatly reducing the experimental screening burden. Feature importance analysis from the ML model provided interpretable structure-activity relationships, emphasizing that particular topological characteristics, in conjunction with charge and electronic properties, are essential determinants of inhibitory activity. Integrated with rigorous *in silico* ADMET profiling and molecular dynamics simulations, these physicochemical insights ensured the prioritization of virtual hits possessing both stable target-binding modes and favorable pharmacokinetic profiles.

Comprehensive biological validation further convinced the applicability of our RF model. The identified hit compound, RF05, characterized by a non-classical molecular scaffold, demonstrated moderate enzymatic inhibition of GSK-3β (IC_{50} = 58.73 μM) and significant anti-inflammatory effect. It reduced pro-inflammatory cytokines (TNF-α and IL-6) and keep low level of cytotoxicity. RF05 as a promising lead scaffold, which can be used to rational structural optimization to obtain the next-generation anti-inflammatory drugs.

Abbreviations

ADMET
Absorption,Distribution,Metabolism,and Excretion,Toxicity
AI
artificial intelligence
Avglpc
atomic polarizability
CADD
Computer-Aided Drug Design
CCK8
Cell Counting Kit-8
ELISA
Enzyme-Linked Immunosorbent Assay
FEL
Free Energy Landscape
FN
False Negatives
FP
False Positives
GB
Gradient Boosting
GSK-3β

Glycogen Synthase Kinase-3 beta
HGBM
Histogram-Based Gradient Boosting
IL-6
interleukin-6
IL-10
interleukin-10
KNN
k-Nearest Neighbors
LINCS
Linear Constraint Solver
LGA
Lamarckian Genetic Algorithm
LGBM
Light Gradient Boost Machine
LogP
lipophilicity
logS
aqueous solubility
MCC
Matthews Correlation Coefficient
MD
Molecular Dynamics
ML
Machine Learning
NB
Naive Bayes (NB)
NC
Negative Control
nHA
number of hydrogen bond acceptors
nHD
number of hydrogen bond donors
nRot and nRig
number of rotatable bonds
PCA
Principal Component Analysis
PR-AUC
Area Under the Precision-Recall Curve
RF

Random Forest
Rg
Radius of Gyration
RMSD
Root Mean Square Deviation
RMSF
Root Mean Square Fluctuation
ROC
Receiver Operating Characteristic
SASA
Solvent Accessible Surface Area
SVMs
Support Vector Machines
TN
True Negatives
TNF-α
tumor necrosis factor
TP
True Positives
TPSA
Topological Polar Surface Area
TTC
Threshold of Toxicological Concern.

Declarations

Supplementary Information. S1 Materials and reagents, S2 Apparatus and measurements.

Acknowledgements

This publication charge is funded by General Project of the Open Research Program at the State Key Laboratory of Neurology and Oncology Drug Development (Contract No. SKLSIM-F-2025131).

Authors' contributions

Wenyuan Zhang: Writing – original draft, Validation, Software, Methodology, Investigation, Formal analysis, Data curation. Shiqi Cheng: Methodology, Investigation, Formal analysis, Data curation. JinJing Zhou: Methodology, Validation, Investigation, Yang Su: Methodology, Validation, Investigation. Shuchen Pei: Validation, Writing – review & editing, Data curation. Jiaming Li: Validation, Investigation. Dan Peng: Validation, Investigation. Fang Liu: Validation, Investigation. Liqun Yang: Writing – review & editing, Validation, Supervision, Conceptualization. Yao Liu: Supervision, Project administration, Conceptualization, Funding acquisition.

Funding

This work was supported by the General Project of the Open Research Program at the State Key Laboratory of Neurology and Oncology Drug Development (Contract No. SKLSIM-F-2025131), Chongqing Clinical Pharmacy Key Specialties Construction Project, Chongqing Natural Science Foundation Project (Grant Nos. 2024NSCQ-KJFZMSX0151).

Data availability

The protein structures used in this study are publicly available in the Protein Data Bank (PDB) under accession numbers 7B6F. ADMET and drug-likeness prediction data were generated using ADMETlab 3.0 (https://admetlab3.scbdd.com/) and SwissADMET (https://swissadme.ch/) web servers. All generated and analyzed data supporting the findings of this study are included within the article.

Clinical trial number

Not applicable.

Ethics approval and consent to participate

Not applicable.

Consent for publication

Not applicable.

Competing interests

The authors declare no competing financial interests.

References

1. JR, W. Molecular cloning and expression of glycogen synthase kinase-3/factor A. *EMBO J* **1990** *9*(8), 2431-2438.
2. Cheng Z, H. T., Yao J, Wang K, Dong X, Yu F, Huang H, Han M, Liao Q, He S, Lyu W, Li Q. Targeting glycogen synthase kinase-3β for Alzheimer's disease: Recent advances and future Prospects. *Eur J Med Chem* **2024**, *265*, 116065. DOI: 10.1016/j.ejmech.2023.116065.
3. Martelli AM, E. C., Paganelli F, Chiarini F, McCubrey JA. GSK-3: a multifaceted player in acute leukemias. *Leukemia* **2021**, *35* (7), 1829-1842. DOI: 10.1038/s41375-021-01243-z.
4. ter Haar E, C. J., Austen DA, Hsiao HM, Swenson L, Jain J. Structure of GSK3beta reveals a primed phosphorylation mechanism. *Nat Struct Biol* **2001**, *8* (7), 593-596.
5. TL., M. GSK-3: An "Ace" Among Kinases. *Cancer Biother Radiopharm* **2024**, *39* (9), 619-631. DOI: 10.1089/cbr.2024.0025.

6. Thorne CA, W. C., Coster AD, Posner BA, Wu LF, Altschuler SJ. GSK-3 modulates cellular responses to a broad spectrum of kinase inhibitors. *Nat Chem Biol* **2015**, *11* (1), 58-63. DOI: 10.1038/nchembio.1690.
7. Rahmatkar SN, S. D. Decoding the role of neurotrophins in glycogen synthase kinase 3-beta regulation in Alzheimer's disease. *Mol Neurobiol* **2025**, *62* (7), 8603-8623. DOI: 10.1007/s12035-025-04776-x.
8. Teli DM, G. A. Glycogen synthase kinase-3: A potential target for diabetes. *Bioorg Med Chem* **2023**, *92*, 117406. DOI: 10.1016/j.bmc.2023.117406.
9. Nanda SS, H. M., Ju H, Papaefthymiou GC, Yi DK. GSK-3 Inhibitors in the Regulation and Control of Colon Carcinoma. *Curr Drug Targets* **2021**, *22* (13), 1485-1495. DOI: 10.2174/1389450122666210204203950.
10. Zhou H, L. J., Zeng J, Hu B, Fang X, Li L. Inhibition of GSK-3β Alleviates Collagen II-Induced Rheumatoid Arthritis in Rats. *Med Sci Monit* **2016**, *22*, 1047-1052. DOI: 10.12659/MSM.897739.
11. Lee, C.; Kim, K.; Hyun, S.; Hong, S.; Rhee, I. Reprogramming macrophage polarization with a small molecule G3I: Enhancing tumor suppression and inflammation control. *Biomedicine & Pharmacotherapy* **2025**, *191*. DOI: 10.1016/j.biopha.2025.118448.
12. Góral, I.; Wichur, T.; Sługocka, E.; Grygier, P.; Głuch-Lutwin, M.; Mordyl, B.; Honkisz-Orzechowska, E.; Szałaj, N.; Godyń, J.; Panek, D.; et al. Exploring Novel GSK-3β Inhibitors for Anti-Neuroinflammatory and Neuroprotective Effects: Synthesis, Crystallography, Computational Analysis, and Biological Evaluation. *ACS Chemical Neuroscience* **2024**, *15* (17), 3181-3201. DOI: 10.1021/acschemneuro.4c00365.
13. Gong, X.N.; Zhou, Y.X.; Wang, C.Y.; Wang, T.T.; Gao, Z.Y.; Long, W.C.; Li, R.; Cai, L. CPD47, a novel GSK-3β inhibitor, demonstrates antidepressant-like effects via the GSK-3β/β-catenin signaling pathway: Involvement of neurogenesis promotion and neuroinflammation inhibition. *International Immunopharmacology* **2026**, *169*. DOI: 10.1016/j.intimp.2025.116065.
14. Lovestone, S.; Boada, M.; Dubois, B.; Hüll, M.; Rinne, J. O.; Huppertz, H.-J.; Calero, M.; Andrés, M. V.; Gómez-Carrillo, B.; León, T.; et al. A Phase II Trial of Tideglusib in Alzheimer's Disease. *J Alzheimers Dis* **2015**, *45* (1), 75-88. DOI: 10.3233/jad-141959.
15. Li, J.; Ma, S.; Chen, J.; Hu, K.; Li, Y.; Zhang, Z.; Su, Z.; Woodgett, J. R.; Li, M.; Huang, Q. GSK-3β contributes to Parkinsonian dopaminergic neuron death: Evidence from conditional knockout mice and Tideglusib. *Front Mol Neurosci* **2020**, *13*, 81. DOI: 10.3389/fnmol.2020.00081.
16. Martínez-González, L.; Gonzalo-Consuegra, C.; Gómez-Almería, M.; Porras, G.; de Lago, E.; Martín-Requero, Á.; Martínez, A. Tideglusib, a Non-ATP Competitive Inhibitor of GSK-3β as a Drug Candidate for the Treatment of Amyotrophic Lateral Sclerosis. *Int J Mol Sci* **2021**, *22* (16), 8975. DOI: 10.3390/ijms22168975.
17. Joshi, B.; Singh, D.; Wasan, H.; Sharma, U.; Reeta, K. H. Tideglusib Ameliorates Ischemia/Reperfusion Damage by Inhibiting GSK-3β and Apoptosis in Rat Model of Ischemic Stroke. *J Stroke Cerebrovasc Dis* **2022**, *31* (4). DOI: 10.1016/j.jstrokecerebrovasdis.2022.106349.

18. Xun, Q.-Q.; Zhang, J.; Feng, L.; Ma, Y.-Y.; Li, Y.; Shi, X.-L. Identification of a novel pyrrolo[2,3-b]pyridine compound as a potent glycogen synthase kinase 3β inhibitor for treating Alzheimer's disease. *Journal of Enzyme Inhibition and Medicinal Chemistry* **2025**, *40* (1). DOI: 10.1080/14756366.2025.2466846.
19. Xu J, Y. Z., Zhao F, Pan C, Yang J, Zhang Z, Dong L, Dong Y. Design, synthesis, and biological evaluation of novel GSK-3β covalent inhibitors for cancer treatment. *Bioorg Chem* **2025**, *164*, 108856. DOI: 10.1016/j.bioorg.2025.108856.
20. Madarakhandi, A.; Kumar, S.; Teraiya, N.; Schols, D.; Vastrad, S. J.; Shyamjith, P.; Choudhary, B.; Rai, A.; Karki, S. S. Design, synthesis and anticancer evaluation of novel hydrazide-2-oxindole analogues as GSK-3β kinase inhibitors. *RSC Advances* **2025**, *15* (30), 24650-24667. DOI: 10.1039/d5ra01063b.
21. Sukanya S, B.-S. A., Singh Choudhary B, Kumar S, Pérez B, Leandro Martínez Rodríguez A, Brea J, Griñán-Ferré C, Malik R. Design, synthesis, and biological evaluation of tetrahydropyrimidine analogue as GSK-3β/Aβ aggregation inhibitor and anti-Alzheimer's agent. *Bioorg Chem* **2024**, *153*, 107811. DOI: 10.1016/j.bioorg.2024.107811.
22. Xie, Y.; Chen, C.; Lin, S.; Yu, X.; Ye, S.; Chen, X.; Ouyang, N.; Xiong, W.; Li, C.; Xu, C.; et al. Design, synthesis and anti-AD effects of dual inhibitor targeting glutaminyl cyclase/GSK-3β. *Eur J Med Chem* **2023**, *248*, 115089. DOI: 10.1016/j.ejmech.2023.115089.
23. A, L. Machine-learning approaches in drug discovery: methods and applications. *Drug Discov Today* **2015**, *20* (3), 318-331. DOI: 10.1016/j.drudis.2014.10.012.
24. Svetnik V, L. A., Tong C, Culberson JC, Sheridan RP, Feuston BP. Random Forest: A Classification and Regression Tool for Compound Classification and QSAR Modeling. *Chem Inf Comput Sci* **2003**, *43* (6), 1947-1958.
25. Kim S, C. J., Cheng T, Gindulyte A, He J, He S, Li Q, Shoemaker BA, Thiessen PA, Yu B, Zaslavsky L, Zhang J, Bolton EE. PubChem 2025 update. *Nucleic Acids Res* **2025**, *53* (D1), D1516-D1525. DOI: 10.1093/nar/gkae1059.
26. Bento, A. P.; Hersey, A.; Félix, E.; Landrum, G.; Gaulton, A.; Atkinson, F.; Bellis, L. J.; De Veij, M.; Leach, A. R. An open source chemical structure curation pipeline using RDKit. *J Cheminform* **2020**, *12* (1), 51. DOI: 10.1186/s13321-020-00456-1.
27. Nandi S, B. M. Importance of Kier-Hall topological indices in the QSAR of anticancer drug design. *Curr Comput Aided Drug Des* **2012**, *8* (2), 159-170.
28. Kluyver, T.; Ragan-Kelley, B.; eacute; rez, F.; Granger, B.; Bussonnier, M.; Frederic, J.; Kelley, K.; Hamrick, J.; Grout, J.; et al. Jupyter Notebooks – a publishing format for reproducible computational workflows. In *Positioning and Power in Academic Publishing: Players, Agents and Agendas*, 2016.
29. Patlewicz, G.; Jeliazkova, N.; Safford, R. J.; Worth, A. P.; Aleksiev, B. An evaluation of the implementation of the Cramer classification scheme in the Toxtree software. *SAR QSAR Environ Res* **2008**, *19* (5-6), 495-524. DOI: 10.1080/10629360802083871.

30. Fu, L.; Shi, S.; Yi, J.; Wang, N.; He, Y.; Wu, Z.; Peng, J.; Deng, Y.; Wang, W.; Wu, C.; et al. ADMETlab 3.0: an updated comprehensive online ADMET prediction platform enhanced with broader coverage, improved performance, API functionality and decision support. *Nucleic Acids Res* **2024**, *52* (W1), W422-W431. DOI: 10.1093/nar/gkae236.
31. Trott, O.; Olson, A. J. AutoDock Vina: Improving the speed and accuracy of docking with a new scoring function, efficient optimization, and multithreading. *Journal of Computational Chemistry* **2009**, *31* (2), 455-461. DOI: 10.1002/jcc.21334.
32. Morris, G. M.; Huey, R.; Lindstrom, W.; Sanner, M. F.; Belew, R. K.; Goodsell, D. S.; Olson, A. J. AutoDock4 and AutoDockTools4: Automated docking with selective receptor flexibility. *Journal of Computational Chemistry* **2009**, *30* (16), 2785-2791. DOI: 10.1002/jcc.21256.
33. Andreev, S.; Pantsar, T.; Tesch, R.; Kahlke, N.; El-Gokha, A.; Ansideri, F.; Grätz, L.; Romasco, J.; Sita, G.; Geibel, C.; et al. Addressing a Trapped High-Energy Water: Design and Synthesis of Highly Potent Pyrimidoindole-Based Glycogen Synthase Kinase-3β Inhibitors. *Journal of Medicinal Chemistry* **2021**, *65* (2), 1283-1301. DOI: 10.1021/acs.jmedchem.0c02146.
34. Papaleo, E.; Mereghetti, P.; Fantucci, P.; Grandori, R.; De Gioia, L. Free-energy landscape, principal component analysis, and structural clustering to identify representative conformations from molecular dynamics simulations: The myoglobin case. *Journal of Molecular Graphics and Modelling* **2009**, *27* (8), 889-899. DOI: 10.1016/j.jmgm.2009.01.006.
35. Liang, J.-W.; Wang, M.-Y.; Wang, S.; Li, S.-L.; Li, W.-Q.; Meng, F.-H. Identification of novel CDK2 inhibitors by a multistage virtual screening method based on SVM, pharmacophore and docking model. *J Enzyme Inhib Med Chem* **2019**, *35* (1), 235-244. DOI: 10.1080/14756366.2019.1693702.
36. Arian, R.; Hariri, A.; Mehridehnavi, A.; Fassihi, A.; Ghasemi, F. Protein kinase inhibitors' classification using K-Nearest neighbor algorithm. *Comput Biol Chem* **2020**, *86*. DOI: 10.1016/j.compbiolchem.2020.107269.
37. Chen, S.; Webb, G. I.; Liu, L.; Ma, X. A novel selective naïve Bayes algorithm. *Knowl-Based Syst* **2020**, *192*. DOI: 10.1016/j.knosys.2019.105361.
38. Bentéjac, C.; Csörgő, A.; Martínez-Muñoz, G. A comparative analysis of gradient boosting algorithms. *Artif Intell Rev* **2020**, *54* (3), 1937-1967. DOI: 10.1007/s10462-020-09896-5.
39. Galati, S.; Di Stefano, M.; Bertini, S.; Granchi, C.; Giordano, A.; Gado, F.; Macchia, M.; Tuccinardi, T.; Poli, G. Identification of New GSK3β Inhibitors through a Consensus Machine Learning-Based Virtual Screening. *Int J Mol Sci* **2023**, *24* (24). DOI: 10.3390/ijms242417233.
40. Pirzada, R. H.; Ahmad, B.; Qayyum, N.; Choi, S. Modeling structure–activity relationships with machine learning to identify GSK3-targeted small molecules as potential COVID-19 therapeutics. *Front Endocrinol* **2023**, *14*, 1084327. DOI: 10.3389/fendo.2023.1084327.
41. Strieth-Kalthoff, F.; Sandfort, F.; Segler, M. H. S.; Glorius, F. Machine learning the ropes: principles, applications and directions in synthetic chemistry. *Chem Soc Rev* **2020**, *49* (17), 6154-6168. DOI: 10.1039/c9cs00786e.

42. Vignaux, P. A.; Minerali, E.; Foil, D. H.; Puhl, A. C.; Ekins, S. Machine Learning for Discovery of GSK3β Inhibitors. *ACS Omega* **2020**, *5* (41), 26551-26561. DOI: 10.1021/acsomega.0c03302.
43. Shri, S. R.; Manandhar, S.; Nayak, Y.; Pai, K. S. R. Role of GSK-3β Inhibitors: New Promises and Opportunities for Alzheimer's Disease. *Advanced Pharmaceutical Bulletin* **2023**, *13* (4), 688-700. DOI: 10.34172/apb.2023.071.
44. Chagaleti, B. K.; Saravanan, V.; Vellapandian, C.; Kathiravan, M. K. Exploring cyclin-dependent kinase inhibitors: a comprehensive study in search of CDK-6 inhibitors using a pharmacophore modelling and dynamics approach. *RSC Advances* **2023**, *13* (48), 33770-33785. DOI: 10.1039/d3ra05672d.
45. Chen, J.; Zhang, Z.; Li, H.; Tang, H. Exploring the effect of a series of flavonoids on tyrosinase using integrated enzyme kinetics, multispectroscopic, and molecular modelling analyses. *International Journal of Biological Macromolecules* **2023**, *252*. DOI: 10.1016/j.ijbiomac.2023.126451.
46. Naveed, M.; Ibrahim, S.; Aziz, T.; Asim, M.; Majeed, M. N.; Khan, A. A.; El Hadi Mohamed, R. A.; Alwethaynani, M. S.; Al-Joufi, F. A.; Fallatah, D. Computational drug design for neurosyphilis disease by targeting Phosphoglycerate Kinase in Treponema pallidum with enhanced binding affinity and reduced toxicity. *Scientific Reports* **2025**, *15* (1). DOI: 10.1038/s41598-025-94054-6.

Figures

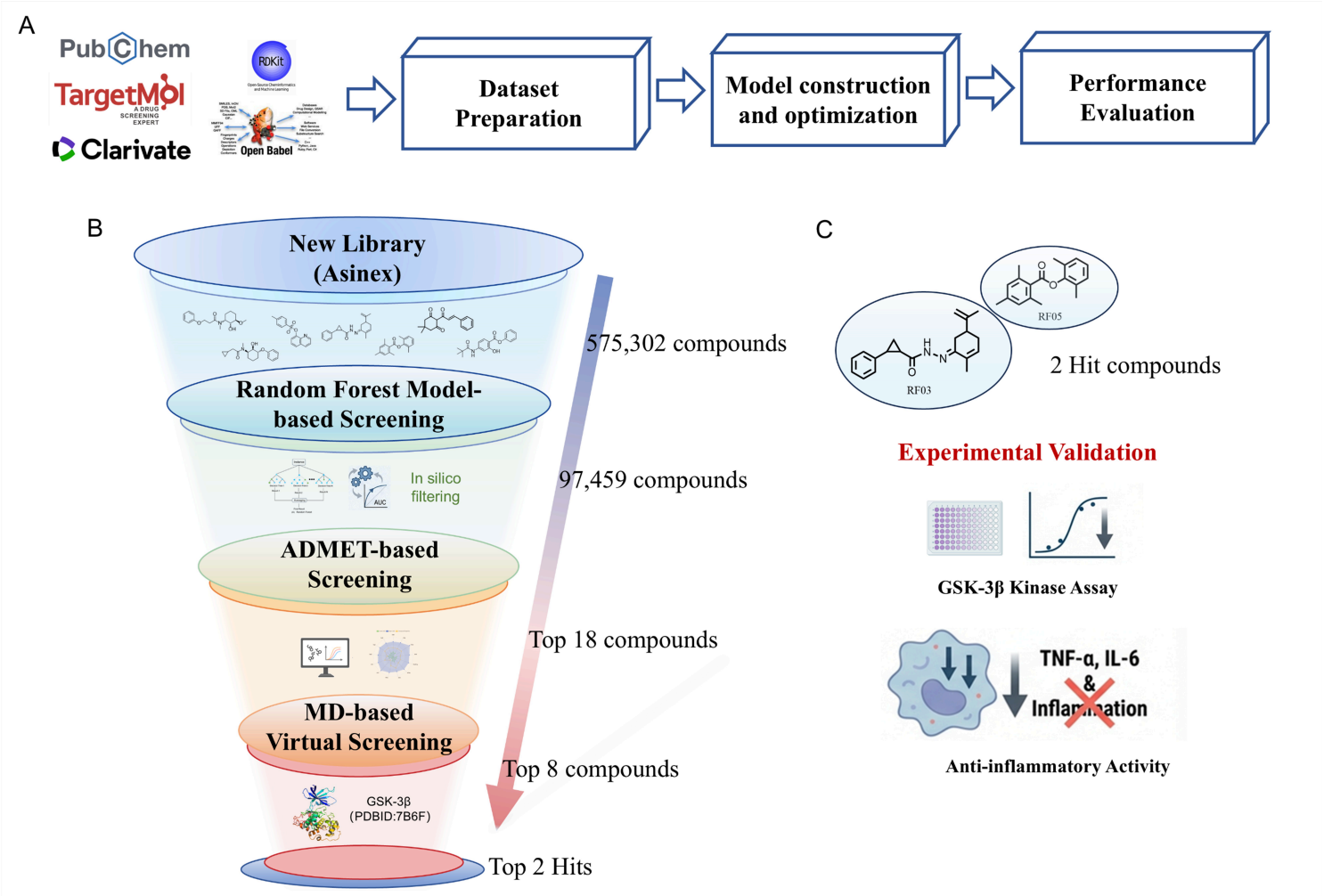


Figure 1

(A) Flowchart for building models; (B) Flowchart for screening; (C) Experimental validation of hit compounds.

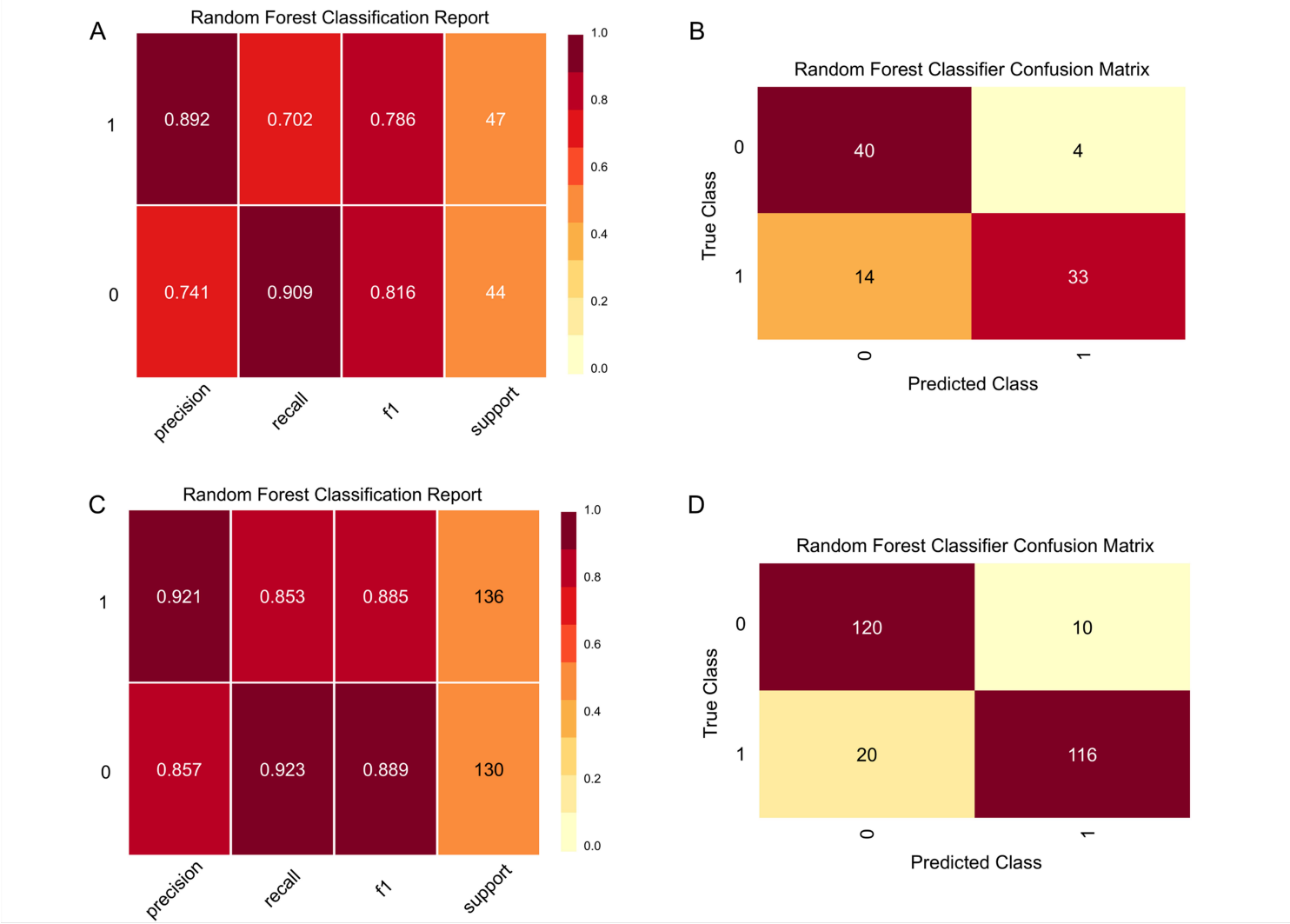


Figure 2

Performance evaluation of the Random Forest classifier for GSK-3 inhibitor screening across validation sets of varying scales. (A, B) Classification report heatmap and confusion matrix derived from the preliminary validation set (n=91). The heatmap visualizes Precision, Recall, and F1-scores, with color intensity corresponding to the metric value. Class 1 designates active GSK-3 inhibitors, while Class 0 denotes inactive compounds. (C, D). Classification report heatmap and confusion matrix for the extended independent validation set (n=266). Value within the confusion matrices represent the counts of True Negatives (top-left), False Positives (top-right), False Negatives (bottom-left), and True Positives (bottom-right). Comparative analysis reveals that with an increased validation sample size, the model maintains high precision while exhibiting a significant improvement in recall, demonstrating superior generalization capability and robustness.

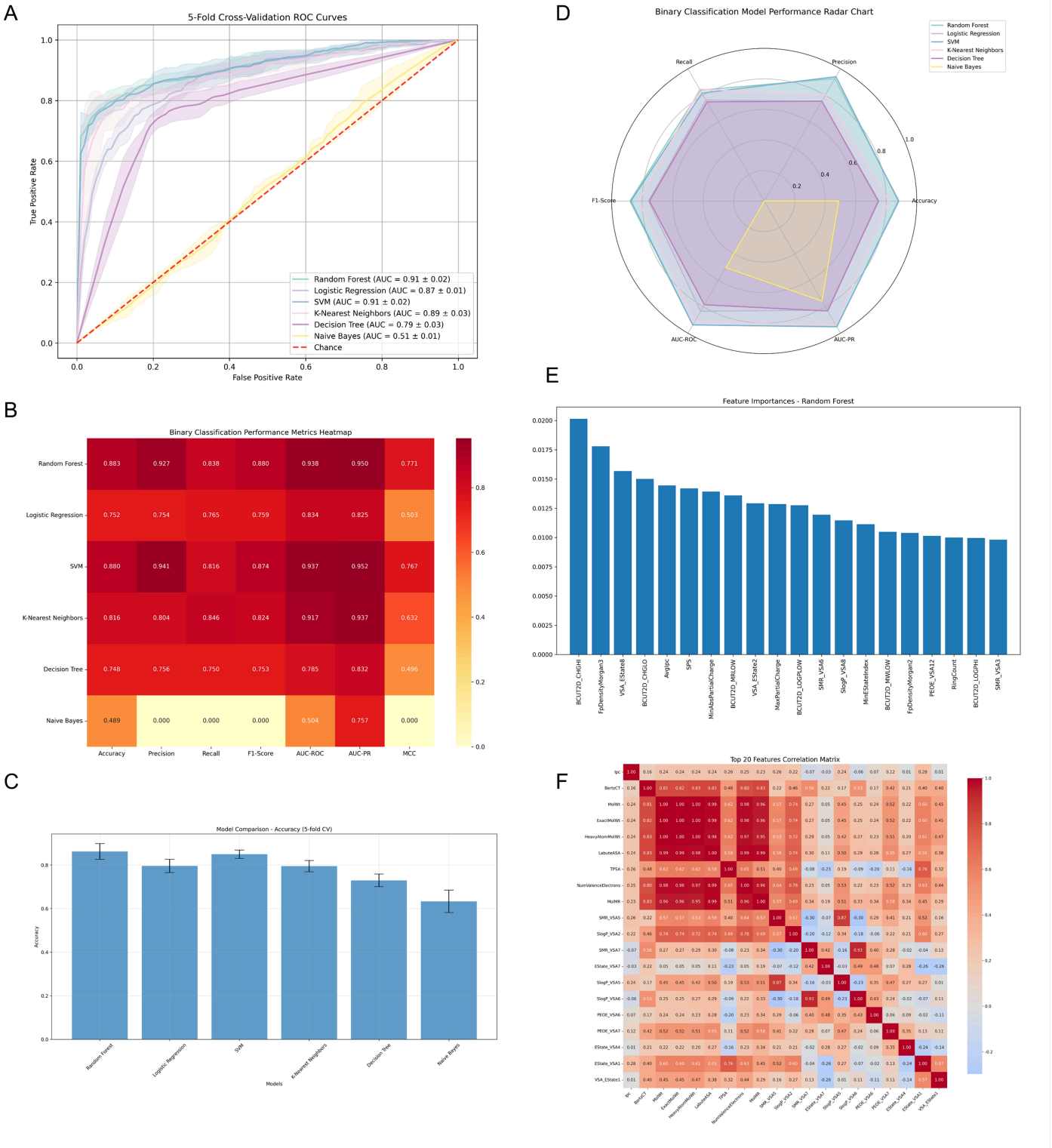


Figure 3

(A) Receiver Operating Characteristic (ROC) curve of the optimized Random Forest model; (B) binary classification model performance metrics heatmap; (C) Accuracy of Random Forest, Logistic Regression, SVM, K-Nearest Neighbors, Decision Tree and Naïve Bayes; (D) Binary classification model performance radar chart; (E) Top 20 descriptors in constructed RF model; (F) Visualization of top 20 RF important features and their correlation with active compounds.

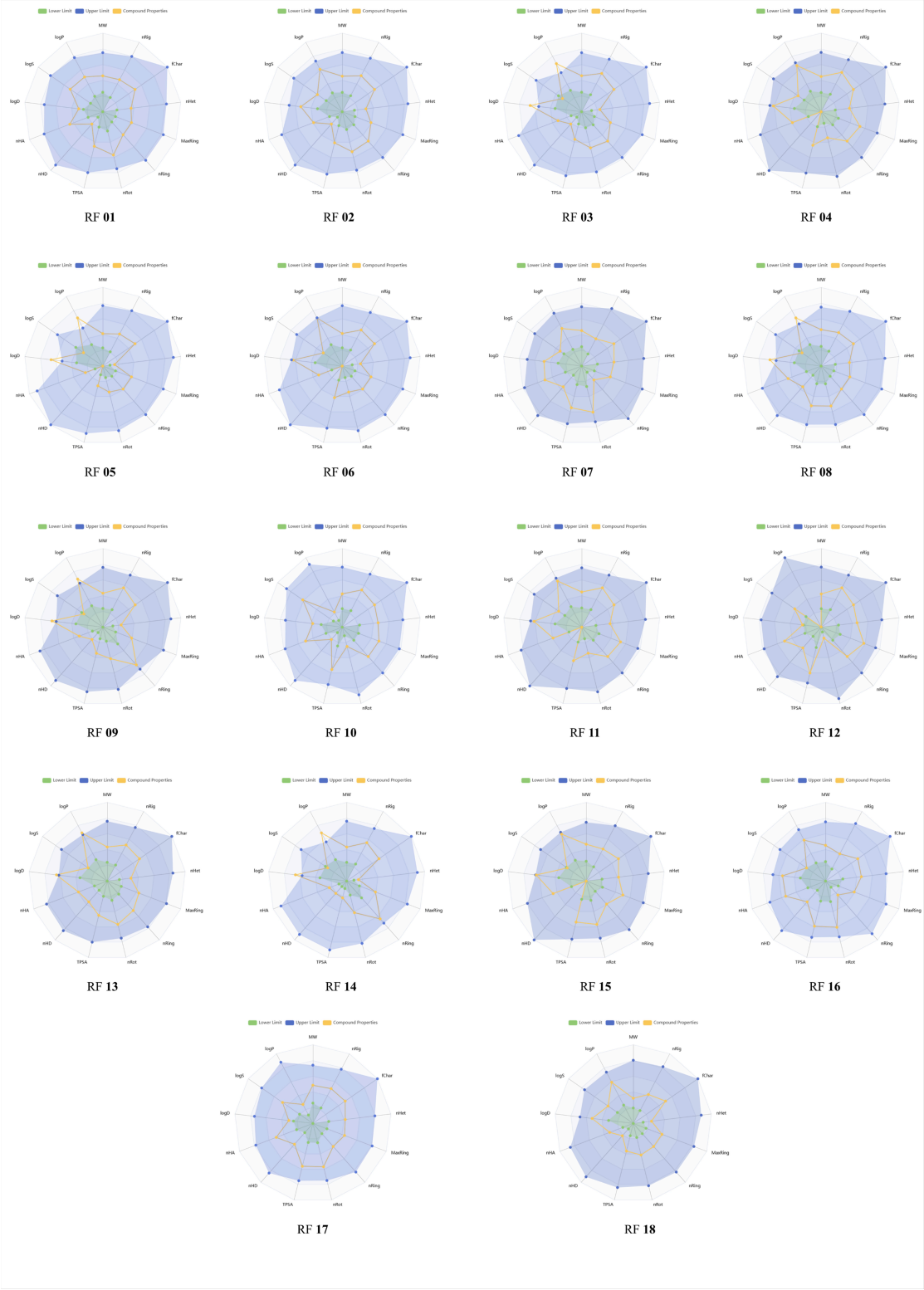


Figure 4

Radar Chart of Top 18 compounds.

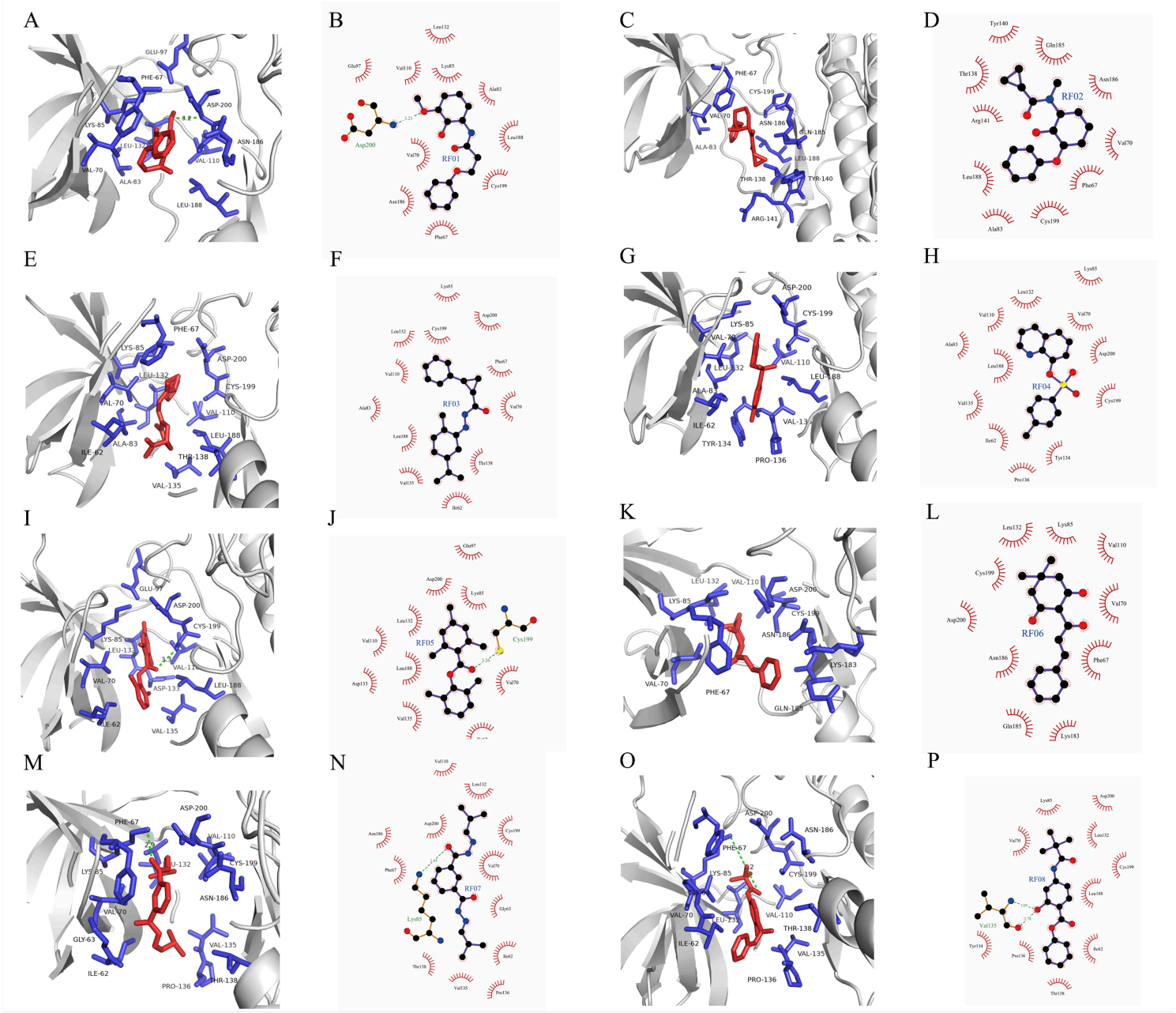


Figure 5

3D and 2D binding interactions of GSK-3β structure with (A, B) RF01, (C, D) RF02, (E, F) RF03, (G, H) RF04, (I, J) RF05, (K, L) RF06, (M, N) RF07, and (O, P) RF08.

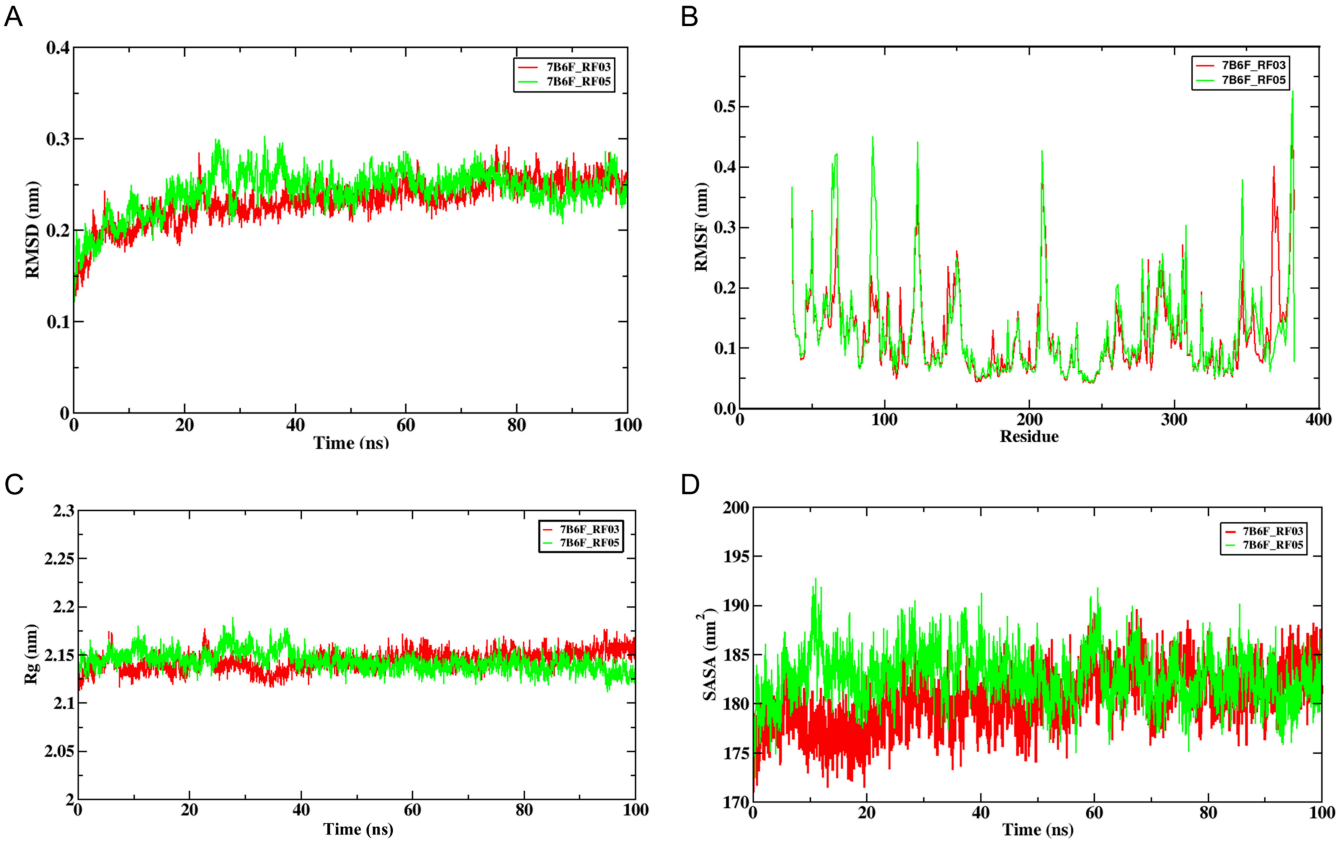


Figure 6

MD analysis of GSK-3β in complex with RF03 and RF05. (A) Mean RMSD, (B) RMSF, (C) Rg, and (D) SASA analysis.

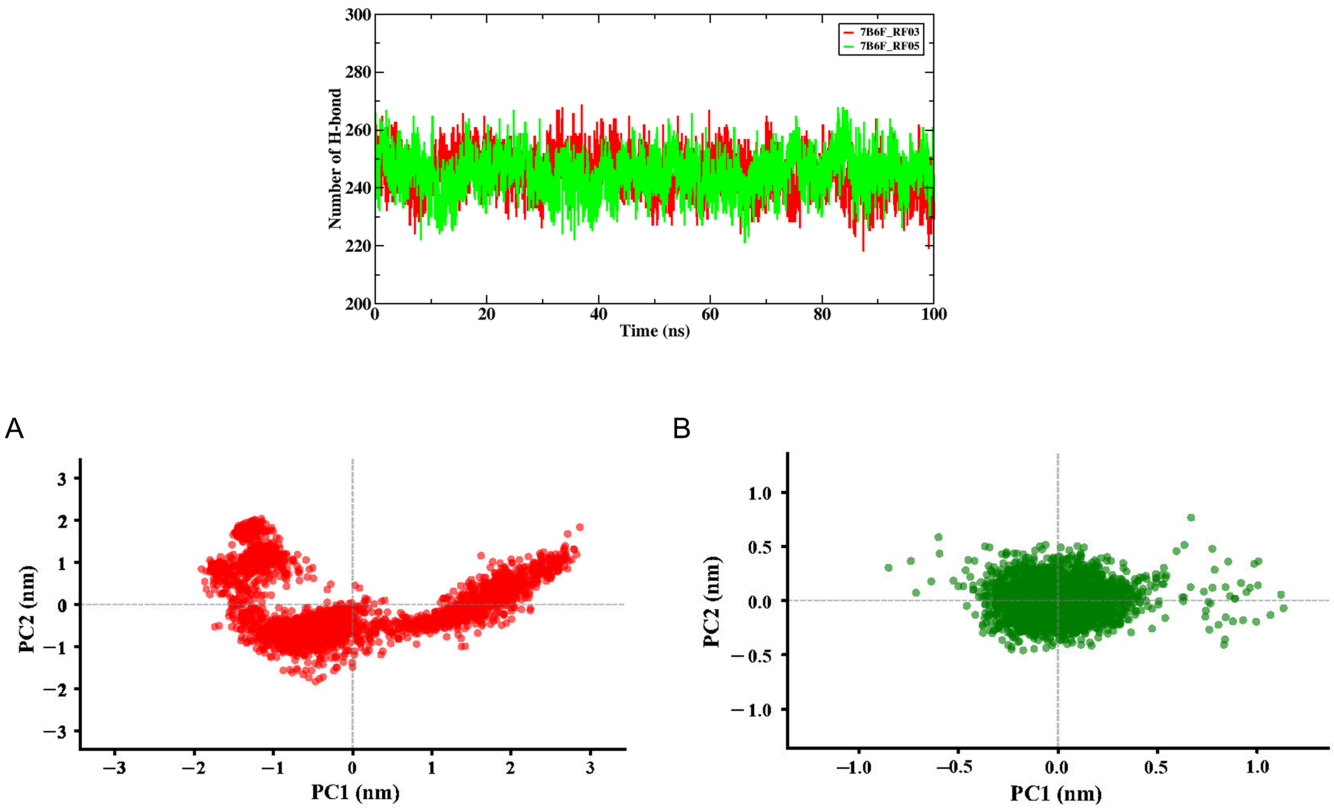


Figure 7

Plot plots of the mean principal component analysis of RF03 (A) and RF05 (B), exploration of conformational and dynamical space during 100 ns simulations.

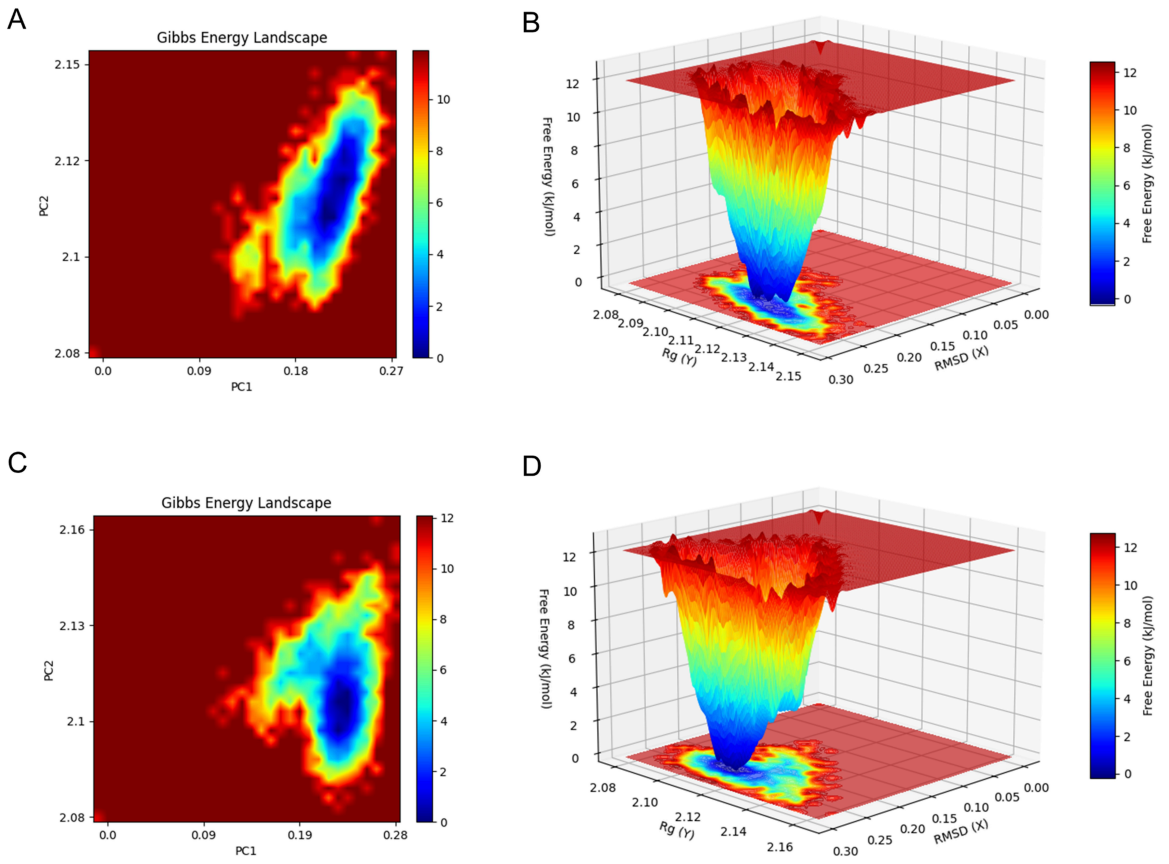


Figure 8

Free energy landscape (FEL) derived from the analysis of GSK-3β protein variations during its interaction with: (A, B) RF03, (C, D) RF05. (A, C) represent 2D projections of the free energy surface based on the first two principal components. The deep blue areas show the conformational states with the least energy (global minima). (B, D) show 3D landscapes based on the Root Mean Square Deviation (RMSD) and Radius of Gyration (Rg). The deep blue "valleys" on these plots show the energy basins that are the most stable thermodynamically.

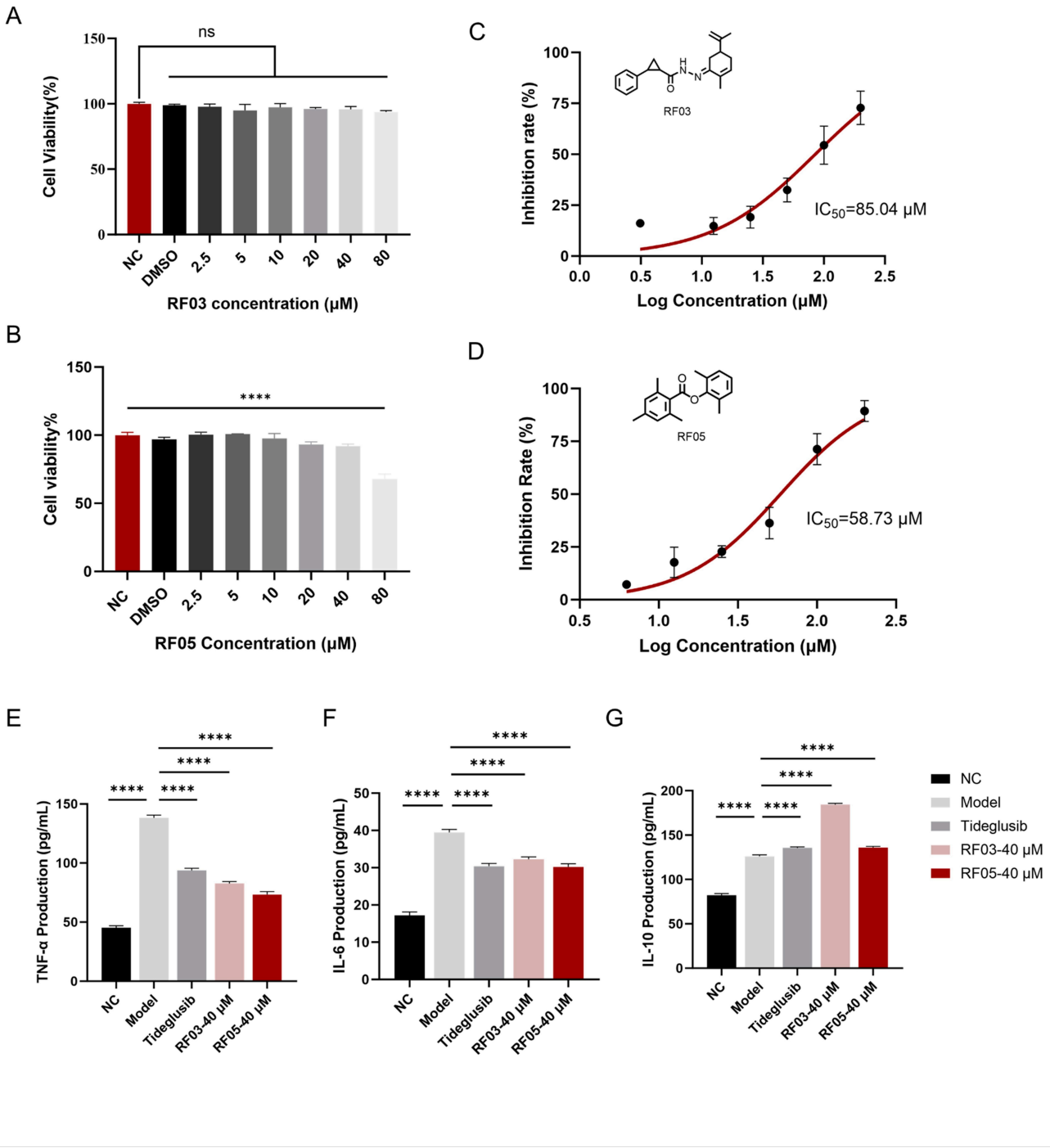


Figure 9

(A, B) The effect of compounds RF03 and RF05 at different concentrations on cell viability; (C, D) Plot of half inhibitory concentrations of RF03 and RF05; (E) The effect of compounds RF03 and RF05 on the production of TNF-α; (F) The effect of compounds RF03 and RF05 on the production of IL-6; (G) The effect of compounds RF03 and RF05 on the production of IL-10.

Supplementary Files

This is a list of supplementary files associated with this preprint. Click to download.

- Supplementarymaterial.docx